Article:
Qin, Y., Li, G.-J., Jia, C. et al. (2024) Investigation of inter-turn short-circuit fault of PM machines using PWM voltage-based modeling. IEEE Transactions on Transportation Electrification, 10 (1). pp. 1324-1334. ISSN: 2332-7782

https://doi.org/10.1109/TTE.2023.3277209

Investigation of Inter-Turn Short-Circuit Fault of PM Machines using PWM Voltage-based Modeling

Y. Qin, *Student Member, IEEE*, G. J. Li, *Senior Member, IEEE,* C. J. Jia, and P. McKeever

***Abstract*—This paper aims to develop an analytical fault model based on PWM voltages for permanent magnet (PM) machines with inter-turn short-circuit fault. Using PWM voltage-based modelling is mainly because the PM machines are commonly driven by PWM inverters. This model is more accurate compared to the ones that use sinewave voltages as inputs as the latter neglect the PWM harmonics in the fault current. However, the investigation in this paper showed that, depending on the DC bus voltage and switching frequency, the PWM harmonic component could be more than 50% of the fundamental component in the fault current, therefore, cannot be neglected. Based on this developed fault model, the characteristics of the fault current have been explored first, which revealed that the back-EMFs mainly contribute to the fundamental component of the fault current, whilst the PWM voltages not only affect its fundamental component but also the PWM harmonics. Secondly, the factors such as DC bus voltage, switching frequency, number of short-circuited turns and different coil connections affecting the PWM ripple components in the phase current and the fault current have also been investigated. Finally, the MATLAB/Simulink simulations based on the developed fault model have been fully validated by a series of tests.**

***Index Terms*—Fault modelling, inter-turn short circuit fault, parallel/series coils, PM machines, PWM ripple current.**

I. INTRODUCTION

Due to their excellent performances such as high torque/power density and high efficiency [1], permanent magnet (PM) machines have received more and more attention both in academy and industry. In addition, thanks to the significant improvement in the machine design, control performance and manufacture, PM machines are being widely employed in the safety-critical applications, e.g., offshore wind power and aerospace [2]. For such applications, fault tolerant capability is also pivotal as without it, a local fault might escalate and potentially lead to a total system failure. From the existing literature, it is known that faults in the PM machines can be classified into two main categories, i.e., mechanical and electromagnetic faults [3]. Amongst all these faults, the inter-turn short circuit (ITSC) fault is often regarded as the commonest and the worst fault, which accounts for 30-40% of total failures [4]. Factors such as electrical loading, thermal stress and environmental contamination attribute to the winding insulation degradation, which will eventually lead to ITSC fault [5]. Machines with ITSC fault can generate very large fault current, which may be 30 times of the rated current because of its low impedance in the faulted circuit loop. As a result, such high fault current in the faulted turns can lead to local overheating and will further damage the winding insulation, leading to an entire phase breakdown [6]. In addition, this large fault current could also lead to the irreversible demagnetization of PMs [7], [8]. As the ITSC faults pose serious risks to the reliability of the PM machines, extensive research has been carried out in both academia and industry to find effective ways of coping with them. To this end, fault modelling has been deemed critical as it allows predicting the machine behavior and performance under ITSC faults. In addition, it can also provide theoretical support required to evaluate the consequences caused by this severe fault. Furthermore, to some extent, accurate fault models can help develop adequate fault diagnostic methods [9] [10] and fault mitigation strategies [6] [11].

Given the importance, numerous works focusing on fault modeling have been presented in the literature, and the fault modelling methods are often divided into two main categories such as analytical approach and finite-element method (FEM). In general, the former requires much less computation time but suffers from relatively lower accuracy than the latter. In [12], a general analytical model with ITSC fault for multiphase fault-tolerant PM machines has been developed, in which a novel T-type equivalent circuit has been adopted. In [13], based on the principles of magnetically coupled circuit theory, electromechanical energy conversion, and reference frame theory, a mathematical model for an interior-mounted line start PM machine with ITSC fault was developed. In [14], a dynamic model for the surface-mounted PM machines with ITSC fault has been established using two *dq*-synchronous reference frames (positive and negative sequence frame). However, for the multipole machines, this fault model is less accurate since it neglects the flux coupling between the faulted coil and the other healthy coils in the same phase. An improved fault model for series/parallel coils considering the flux coupling between the faulted coil and the other healthy coils in the same phase has been derived in [15]. In [16], the classical *d*- and *q*-axis theory was employed to derive the parametric model of PM machines under ITSC fault. However, this proposed fault model neglected the effects of space harmonics, and an improved model considering the space harmonics was presented in [17]. In addition to the above analytical approach, researchers also continuously explore the possibility of developing fault models using direct FEM approach due to its excellent accuracy in predicting the electromagnetic performance of the electrical machines [18-20]. As a trade-off between the computation time

Manuscript received October 10, 2022; revised February 24, 2023 and April 04, 2023, and accepted May 12, 2023. (Corresponding author: Guang-Jin Li)

Ying Qin and Guang-Jin Li are with the Department of Electronic and Electrical Engineering, University of Sheffield, Sheffield, S1 3JD, U.K. (e-mail: yqin27@sheffield.ac.uk; g.li@sheffield.ac.uk).

ChunJiang Jia and Paul McKeever are with Offshore, Renewable Energy Catapult, Offshore House, Albert Street, Blyth, Northumberland, NE24 1LZ, UK. (e-mail: chunjiang.jia@ore.catapult.org.uk; paul.mckeever@ore.catapult.org.uk).

and the accuracy of the fault model, a new semi-analytical model for interior PM (IPM) machines with ITSC faults has been developed [21]. In [21], the transient model of the IPM machines with ITSC faults used the *dq*-axis flux linkage map obtained from FEM model in healthy condition and the analytical equations under the ITSC fault condition. Therefore, it combined the advantages of both the analytical and FEM approaches.

It is worth noting that all the models mentioned above used sinewave voltages as inputs to the electrical machines, which cannot fully account for the effects of PWM harmonics in the fault current. However, the investigations in this paper showed that the dominant PWM ripple component in the short-circuit current could reach more than 50% of the fundamental component. In this case, using the aforementioned fault models in the literature would seriously underestimate the short-circuit current and the extra copper loss (and thermal stress) introduced by the PWM ripple component in the faulted turns. To address these shortcomings, this paper proposes a more accurate fault model considering the effects of the drives by using the PWM voltages as inputs to the PM machines. Based on the developed fault model, the characteristics of fault current can be comprehensively investigated. In addition, the developed model can be used to explore the factors such as the DC bus voltage, switching frequency, number of short-circuited turns and different coil connections that affect the PWM ripple component of the fault current. This has rarely been studied in the literature and will be the main novelty and contribution of this paper.

The rest of this paper is structured as shown in Fig. 1. In section II, a PWM-voltage based model for PM machine under ITSC fault is developed, which has been validated by a series of experiments. In section III, the factors such as back-EMF and PWM voltages contributing to the fundamental component of fault current have been investigated. In section IV, the contributors such as DC bus voltage, switching frequency, number of short-circuited turns and different coil connections to the PWM ripple component of fault current are discussed. Finally, some conclusions are drawn in Section V.

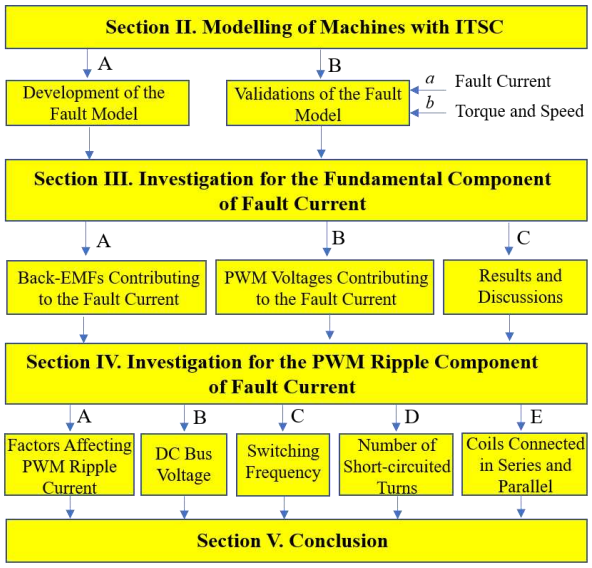

Fig. 1 Flowchart summarizing the structure of this paper.

II. Modeling of Machines with ITSC

A schematic representing a PM machine driven by a 3-phase voltage source inverter (VSI) is shown in Fig. 2. The signals output from the inverter, which are the inputs to the PM machine, are labeled as V_{dslA}, V_{dslB} and V_{dslC}. They represent the PWM voltages of the 3-phase windings. As example, each phase of the investigated PM machine has two coils connected in parallel. However, it is worth noting that the model developed in this paper can be easily extended to other number of parallel connected coils and also coils connected in series. Coils connected in parallel can reduce the back electromotive force (EMF) per phase, which is often used in kW level PM machine as an effective way to increase rotor velocity under a certain voltage level [22]. The results of PM machines with parallel coils will be compared against the ones with series coils in section IV.E.

It is observed from Fig. 2 that a_1, a_2, b_1, b_2, c_1 and c_2 represent the coils of the 3-phase windings, i_a, i_b and i_c are the 3-phase currents. For the analyses in this paper, it is assumed that the ITSC fault occurs in a_1 coil. Here, i_{p1} and i_f (fault current) denote the current flowing through the remaining healthy turns and the faulted turns in a_1 coil, respectively, and i_{p2} is the current in coil a_2. R_f is the contact resistance and v_n is the common mode voltage. Under healthy condition, the relationship between i_a, i_{p1} and i_{p2} is $i_{p1} = i_{p2} = i_a/2$. However, this is not the case when an ITSC fault occurs since the impedance of the remaining healthy turns of the coil a_1 is not equal to that of the coil a_2. It is worth noting that this paper focuses on analyzing the full short circuit stage. Therefore, the short-circuited turns and healthy turns are in two separate electrical circuits with zero contact resistance. The parameters for this investigated machine are given in TABLE I, which will be used for the analyses in the following sections.

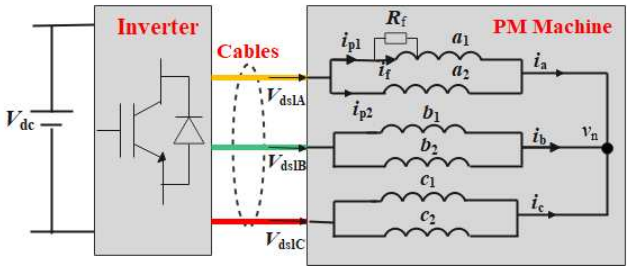

Fig. 2 PM machine with parallel coils under ITSC fault in phase A.

TABLE I PARAMETERS OF THE HEALTHY PM MACHINE UNDER THE HEALTHY CONDITION.

N° of phases	3	Phase resistance (mΩ)	112
N° of poles	8	Phase inductance (μH)	67.5
N° of slots	6	Cable resistance (mΩ)	60
N° of turns per coil	24	Cable inductance (μH)	0.6
PM flux (mWb)	2.972	Contact resistance (mΩ)	0

A. Development of the Fault Model

In this paper, unless specifically highlighted, the PWM ripple current refers to PWM ripple component in the fault current. The equation describing the relationship between voltages and currents under ITSC fault can be written as (1), which is developed by using the PWM voltages as inputs to the PM machines. As a result, the impact of the drives on the fault performance such as the PWM ripple current can be accounted

for. Compared with the fault model in [15], (1) also considers the effects of common model voltage, which exists at the neutral point and cannot be neglected. In addition, to obtain a more accurate fault model, (1) accounts for the influence of the cable resistance (R_{Cable}) not their inductances (L_{cable}). This is because the cables mainly exhibit a resistive characteristic and their inductances are significantly smaller than the total self-inductance of each phase, as shown in TABLE I. It is worth noting that based on the measured parameters, as listed in TABLE I, and the fault ratio (x), the elements in matrix $\boldsymbol{L}$ and $\boldsymbol{R}$ can be obtained according to the work presented in [15].

$$\boldsymbol{L}\frac{d}{dt}\begin{bmatrix} i_{p1} \\ i_{p2} \\ i_b \\ i_c \\ i_f \end{bmatrix} = \begin{bmatrix} v_{\text{Adsl}} \\ v_{\text{Adsl}} \\ v_{Bdsl} \\ v_{Cdsl} \\ 0 \end{bmatrix} - \boldsymbol{R}\begin{bmatrix} i_{p1} \\ i_{p2} \\ i_b \\ i_c \\ i_f \end{bmatrix} - \begin{bmatrix} e_{ah} \\ e_a \\ e_b \\ e_c \\ e_{af} \end{bmatrix} - \begin{bmatrix} 1 \\ 1 \\ 1 \\ 1 \\ 0 \end{bmatrix} v_{\text{n}} \tag{1}$$

with

$$\boldsymbol{L} = \begin{bmatrix} L_{s11} & M_{s12} & M_{s13} & M_{s14} & M_{s15} \\ M_{s21} & L_{s22} & M_{s23} & M_{s24} & M_{s25} \\ M_{s31} & M_{s32} & L_{s33} & M_{s34} & M_{s35} \\ M_{s41} & M_{s42} & M_{s43} & L_{s44} & M_{s45} \\ M_{s51} & M_{s52} & M_{s53} & M_{s54} & L_{s55} \end{bmatrix} \tag{2}$$

and

$$\boldsymbol{R} = \begin{bmatrix} R_{s11} + R_{cable} & R_{cable} & 0 & 0 & 0 \\ R_{cable} & R_{s22} + R_{cable} & 0 & 0 & 0 \\ 0 & 0 & R_{s33} + R_{cable} & 0 & 0 \\ 0 & 0 & 0 & R_{s44} + R_{cable} & 0 \\ 0 & 0 & 0 & 0 & R_{s55} \end{bmatrix} \tag{3}$$

where $R_{\text{s}11}$ is the healthy winding resistance of coil a_1. $R_{\text{s}22}$ is the resistance of the coil a_2. $R_{\text{s}33}$ and $R_{\text{s}44}$ are the resistances of the phases B and C. $R_{\text{s}55}$ is the resistances of the faulted turns in the coil a_1. e_{ah} and e_{af} represent the back-EMF of the healthy and faulted turns in the coil a_1, e_{a}, e_{b} and e_c represent the back-EMFs of the phases A, B and C, respectively. $L_{\text{s}11}$ and $L_{\text{s}55}$ are the inductances of the healthy and faulted turns in the coil a_1, $L_{\text{s}22}$ is the self-inductance of the coil a_2, $L_{\text{s}33}$ is the self-inductance of phase B and $L_{\text{s}44}$ is the self-inductances of the phases C. $M_{\text{s}12}$ and $M_{\text{s}21}$ are the mutual inductances between the healthy turns of the coil a_1 and the coil a_2, $M_{\text{s}13}$ and $M_{\text{s}31}$ are the mutual inductances between the healthy turns of the coil a_1 and the phase B, $M_{\text{s}14}$ and $M_{\text{s}41}$ are the mutual inductances between the healthy turns of the coil a_1 and the phase C, and $M_{\text{s}15}$ and $M_{\text{s}51}$ are the mutual inductances between the healthy and faulted turns of the coil a_1. $M_{\text{s}23}$ and $M_{\text{s}32}$ are the mutual inductances between the coil a_2 and the phase B. $M_{\text{s}24}$ and $M_{\text{s}42}$ are the mutual inductances between the coil a_2 and the phase C. $M_{\text{s}25}$ and $M_{\text{s}52}$ are the mutual inductances between the coil a_2 and the short-circuited turns of the coil a_1, and $M_{\text{s}34}$ and $M_{\text{s}43}$ are the mutual inductances between the phases B and C. $M_{\text{s}35}$ and $M_{\text{s}53}$ are the mutual inductances between the phase B and short-circuited turns of the coil a_1, and $M_{\text{s}45}$ and $M_{\text{s}54}$ are the mutual inductances between the phase C and the short-circuited turns of the coil a_1.

For PM machines, the inputs are the PWM voltages, the outputs are the phase currents, and the common mode voltage is an intermediate variable. Therefore, it is necessary to derive v_{n} from (1), which is represented by the PWM voltages and the currents, as described by (4). With (4), (1) can be further derived as (5).

$$v_n = \frac{1}{4}\begin{bmatrix} 1 \\ 1 \\ 1 \\ 1 \\ 0 \end{bmatrix}^T \left\{ \begin{bmatrix} v_{dslA} \\ v_{dslA} \\ v_{dslB} \\ v_{dslC} \\ 0 \end{bmatrix} - \boldsymbol{L}\frac{d}{dt}\begin{bmatrix} i_{p1} \\ i_{p2} \\ i_b \\ i_c \\ i_f \end{bmatrix} - \boldsymbol{R}\begin{bmatrix} i_{p1} \\ i_{p2} \\ i_b \\ i_c \\ i_f \end{bmatrix} - \begin{bmatrix} e_{ah} \\ e_a \\ e_b \\ e_c \\ e_{af} \end{bmatrix} \right\} \tag{4}$$

And

$$\boldsymbol{P_1 L}\frac{d}{dt}\begin{bmatrix} i_{p1} \\ i_{p2} \\ i_b \\ i_c \\ i_f \end{bmatrix} = \boldsymbol{P_1}\begin{bmatrix} v_{\text{Adsl}} \\ v_{\text{Adsl}} \\ v_{Bdsl} \\ v_{Cdsl} \\ 0 \end{bmatrix} - \boldsymbol{P_1 R}\begin{bmatrix} i_{p1} \\ i_{p2} \\ i_b \\ i_c \\ i_f \end{bmatrix} - \begin{bmatrix} 1-x & 0 & 0 \\ 1 & 0 & 0 \\ 0 & 1 & 0 \\ 0 & 0 & 1 \\ x & 0 & 0 \end{bmatrix}\begin{bmatrix} e_a \\ e_b \\ e_c \end{bmatrix} \tag{5}$$

with

$$\boldsymbol{P_1} = \begin{bmatrix} \frac{3}{4} & -\frac{1}{4} & -\frac{1}{4} & -\frac{1}{4} & 0 \\ -\frac{1}{4} & \frac{3}{4} & -\frac{1}{4} & -\frac{1}{4} & 0 \\ -\frac{1}{4} & -\frac{1}{4} & \frac{3}{4} & -\frac{1}{4} & 0 \\ -\frac{1}{4} & -\frac{1}{4} & -\frac{1}{4} & \frac{3}{4} & 0 \\ 0 & 0 & 0 & 0 & 1 \end{bmatrix} \tag{6}$$

and

$$\begin{bmatrix} e_{ah} \\ e_a \\ e_b \\ e_c \\ e_{af} \end{bmatrix} = \begin{bmatrix} 1-x & 0 & 0 \\ 1 & 0 & 0 \\ 0 & 1 & 0 \\ 0 & 0 & 1 \\ x & 0 & 0 \end{bmatrix}\begin{bmatrix} e_a \\ e_b \\ e_c \end{bmatrix} \tag{7}$$

where $x = N_{fault}/N$ is faulted turn ratio of the coil a_1, and N_{fault} and N are the number of faulted turns and the total number of turns of the coil a_1, respectively.

Since the matrix $\boldsymbol{P_1}$ is a singular matrix, no inverse matrix can be obtained, meaning that the currents in (5) will not have unique solutions. To solve this problem, new current and voltage vectors have been constructed to reduce the order of the system from five to four. This has been described in detail in the APPENDIX. It is worth mentioning that the last rows of matrices in (A4), (A5), (A6) and (A7) are all equal to zero, meaning that the value of i_0 is equal to zero. As expected, the order of the system has been successfully reduced by one. As a result, (A3) can be simplified to (8). Based on (8) and (A2), (1) can be derived as (9).

$$\boldsymbol{L_{4\times4}}\frac{d}{dt}\begin{bmatrix} i_\alpha \\ i_\beta \\ i_\gamma \\ i_\delta \end{bmatrix} = -\boldsymbol{R_{4\times4}}\begin{bmatrix} i_\alpha \\ i_\beta \\ i_\gamma \\ i_\delta \end{bmatrix} + \boldsymbol{V_{4\times2}}\begin{bmatrix} v_\alpha \\ v_\beta \end{bmatrix} - \boldsymbol{E_{4\times2}}\begin{bmatrix} e_\alpha \\ e_\beta \end{bmatrix} \tag{8}$$

$$\frac{d}{dt}\begin{bmatrix} i_{p1} \\ i_{p2} \\ i_b \\ i_c \\ i_f \end{bmatrix} = -\boldsymbol{A}\begin{bmatrix} i_{p1} \\ i_{p2} \\ i_b \\ i_c \\ i_f \end{bmatrix} + \boldsymbol{B}\begin{bmatrix} v_{dslA} \\ v_{dslB} \\ v_{dslC} \end{bmatrix} - \boldsymbol{C}\begin{bmatrix} e_a \\ e_b \\ e_c \end{bmatrix} \tag{9}$$

with

$$\begin{cases} \boldsymbol{A} = \boldsymbol{M_1^{-1}}\begin{bmatrix} \boldsymbol{L_{4\times4}^{-1}} \times \boldsymbol{R_{4\times2}} & \boldsymbol{0_{4\times1}} \\ \boldsymbol{0_{1\times2}} & 0 \end{bmatrix}\boldsymbol{M_1} \\ \boldsymbol{B} = \boldsymbol{M_1^{-1}}\begin{bmatrix} \boldsymbol{L_{4\times4}^{-1}} \times \boldsymbol{V_{4\times2}} & \boldsymbol{0_{4\times1}} \\ \boldsymbol{0_{1\times2}} & 0 \end{bmatrix}\boldsymbol{M_2} \\ \boldsymbol{C} = \boldsymbol{M_1^{-1}}\begin{bmatrix} \boldsymbol{L_{4\times4}^{-1}} \times \boldsymbol{E_{4\times2}} & \boldsymbol{0_{4\times1}} \\ \boldsymbol{0_{1\times2}} & 0 \end{bmatrix}\boldsymbol{M_2} \end{cases} \tag{10}$$

where $\boldsymbol{A}$ is a matrix with a dimension of 5×5, and matrices $\boldsymbol{B}$ and $\boldsymbol{C}$ both have a dimension of 5×3.

In (9), the linear transformation method has been adopted to obtain a unique solution for the currents. Meanwhile, this proposed fault model makes analyzing the PWM ripple components in fault currents possible. This is because the PWM voltages are considered as the other voltage source, in addition to back-EMFs, contributing to the fault current. This will be investigated in detail in the following sections. Furthermore, with the obtained currents from (9) and back-EMFs from (7) the electromagnetic torque (T_{em}) and mechanical equations can be expressed as (11) and (12), respectively.

$$T_{em} = \frac{e_{ah} i_{p1} + e_a i_{p2} + e_b i_b + e_c i_c + e_{af} i_f}{\omega_m} \tag{11}$$

$$T_{em} - T_L - T_{damp} = J \frac{d\omega_m}{dt} \tag{12}$$

where T_{em} is the electromagnetic torque and ω_m is the mechanical angular speed. T_L is the load torque, T_{damp} is the damping torque and J is the machine inertia.

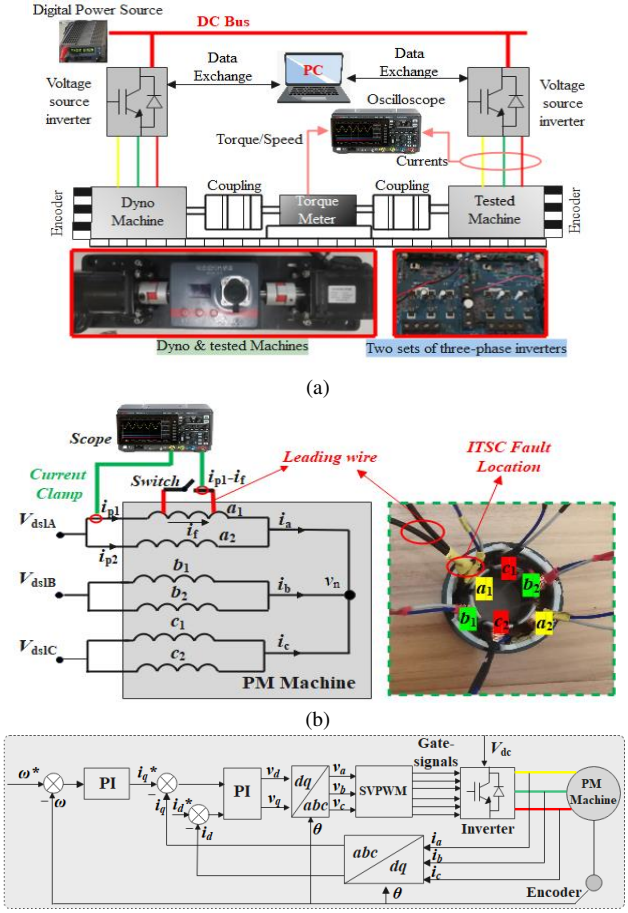

Fig. 3 (a) Test rig, (b) 3-phase circuits with ITSC fault and (C) control diagram of the PM machine system.

B. Validations of the Fault Model

In order to validate the accuracy of the developed fault model, MATLAB/Simulink simulations have been carried out for the PM machine having the specifications shown in TABLE I. In addition, a test rig [see Fig. 3 (a)] has been built to validate the simulations and to investigate the characteristics of the fault current. It can be seen from Fig. 3 (a) that the test rig is composed of a DC power source, two 3-phase MOSFETs-based inverters driving a dyno-machine and the PM prototype machine. Fig. 3 (b) indicates that a thick wire has been soldered to the fault turn taps (coil a_1-faulted coil). Choosing a thick wire is to minimize its introduced impedance into the short-circuited path. A switch is used to short-circuit the wire to simulate an ITSC fault. In addition, Fig. 3 (b) also shows that the fault current (i_f) flowing through the faulted turns is equal to the difference between i_{p1} and (i_{p1}-i_f), which can be directly measured by a current clamp. The encoders mounted at the end of these two machines are used to measure the rotor speed and position, which are the key parameters for the field-oriented control (FOC), seen in Fig. 3 (c). The dyno-machine operates under the speed mode providing stable and constant speeds for the system, while the tested machine with ITSC fault operates under the torque mode. The drive systems in the inverters have a switching frequency of 20kHz and are modulated by the space vector PWM (SVPWM) using a digital signal processor board (DSP28069). It is worth noting that, in the following sections, unless stated otherwise, the ITSC fault is referred to a single turn short-circuit. Different numbers of short-circuited turns have also been investigated (see section IV.D).

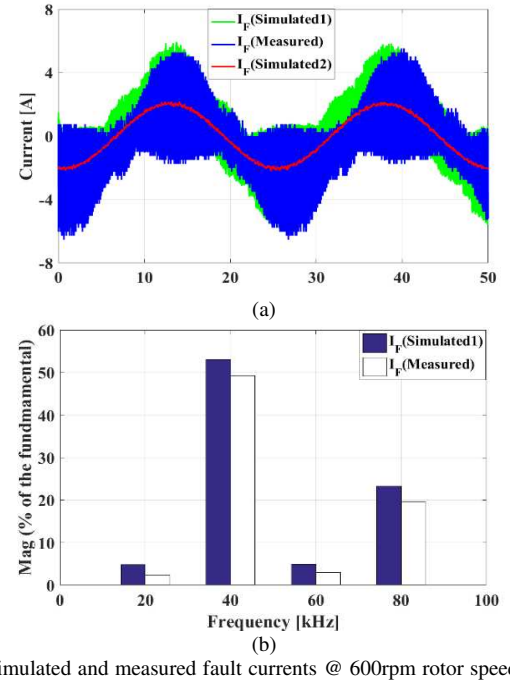

Fig. 4 Simulated and measured fault currents @ 600rpm rotor speed and with the demand currents i_d = 0A and i_q = 10A. (Simulated1: simulated results with PWM voltages as inputs; Simulated2: simulated results with sinewave voltages as inputs). (a) Waveforms and (b) spectra.

a. Fault Current

It is worth noting that, in this section, the rated current (i_d = 0A and i_q = 10A) is used for all the tests. It is observed from Fig. 4 (a) that the simulated fault current [I_F (Simulated1)] from the proposed PWM voltage-based fault model matches well with the measured one [I_F (Measured)]. However, the fault current [I_F (Simulated2)] obtained from the fault model using sinewave voltages as inputs to the PM machine only contains the fundamental component. As a result, it fails to reveal the real electrical behaviors under the ITSC faults. It is worth noting that the dominant PWM harmonics at 40 kHz (twice the switching frequency, i.e., 20kHz) is much larger than other high

frequency harmonics, as shown in Fig. 4 (b). In addition, the PWM ripple component in the fault current can reach around 50% of the fundamental component, and could be even higher depending on the DC bus voltage and switching frequency, which will be elaborated further in sections IV.B and IV.C. Therefore, these PWM harmonics cannot be neglected as they will significantly increase the copper loss in the faulted turns. And as concluded in [23] and [24], the larger the copper loss is, the higher the temperature rise will be.

The fault currents at different rotor speeds have also been simulated and compared against the measured ones, as shown in Fig. 5. Again, a good agreement between the simulated and measured results can be observed, proving the accuracy of the developed fault model.

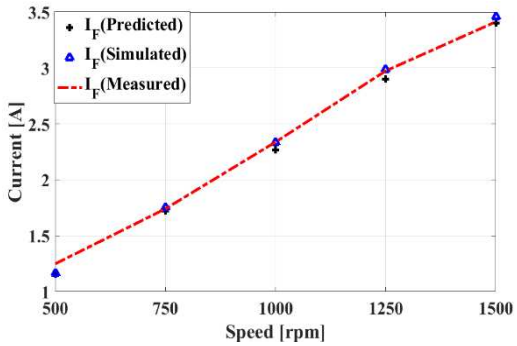

Fig. 5 Predicted, simulated and measured RMS value of fault current *vs* rotor speed. The demand currents are i_d = 0A and i_q = 10A. Predicted results will be described in detail in section III.C.

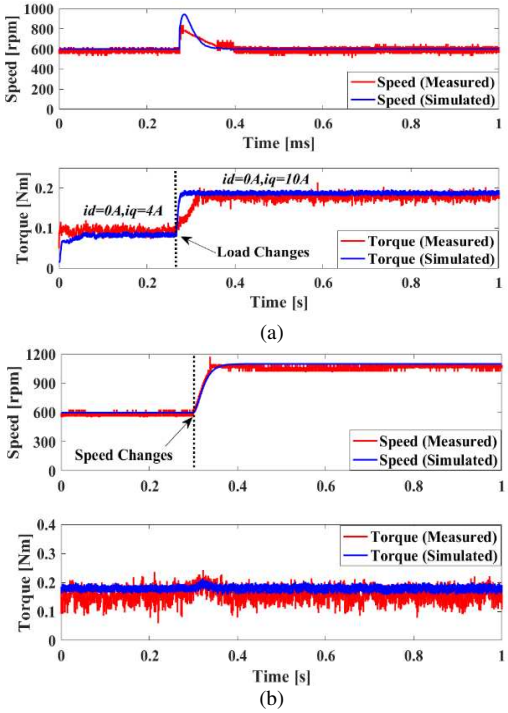

Fig. 6 Simulated and measured speed and torques. (a) Rotor speed is 600rpm and demand currents change from i_d = 0A and i_q = 4A to i_d = 0A and i_q = 10A at around 0.3s. (b) Demand current is i_d = 0A and i_q = 10A and speed changes from 600rpm to 1100rpm at around 0.3s.

b. Torque and Speed

To further validate the developed fault model, rotor speed and torque have been simulated and compared against the measured results, as shown in Fig. 6. It is found that in steady-state, the simulated speed and torque match well with the measured ones. However, in transient-state, i.e., the load changes at around 0.3s as shown in Fig. 6 (a), the simulated speed and torque are slightly different from measured ones. However, this mismatch is within the acceptable range.

III. Investigation for the Fundamental Component of Fault Current

Using the above developed and validated fault model, the characteristics of the fault current can be comprehensively investigated. It is observed from (9) that the PWM voltages and the back-EMFs can be regarded as two independent voltage sources contributing to the fault current. Since the PWM voltages is composed of a series of signals with different frequency, it can not only affect the fundamental component of the fault current but also contribute to the PWM ripple current, which will be elaborated further in section IV. However, the back-EMFs (without PWM harmonics) only affect the fundamental component of the fault current. According to the superposition principle, this section will investigate the impact of these two voltage sources on the fault current separately.

A. Back-EMFs Contributing to the Fault Current

Based on the proposed fault model, the fault current introduced by the back-EMFs in *s*-domain can be derived as

$$i_f(s) = \boldsymbol{A_5 C}\begin{bmatrix} e_a(s) \\ e_b(s) \\ e_c(s) \end{bmatrix} = \begin{bmatrix} f_{eA}(s) \\ f_{eB}(s) \\ f_{eC}(s) \end{bmatrix}^T \begin{bmatrix} e_a(s) \\ e_b(s) \\ e_c(s) \end{bmatrix} \tag{13}$$

where $f_{eA}(s)$ $f_{eB}(s)$ and $f_{eC}(s)$ are the transfer functions of the back-EMFs of phases A, B and C, respectively. $\boldsymbol{A_5}$ is a matrix with a dimension of 1×5, and can be calculated by

$$\begin{aligned} \boldsymbol{A_5} &= [0 \quad 0 \quad 0 \quad 0 \quad 1](\boldsymbol{SI} - \boldsymbol{A})^{-1} \\ &= [a_{51} \quad a_{52} \quad a_{53} \quad a_{54} \quad a_{55}] \end{aligned} \tag{14}$$

where a_{51}, a_{52}, a_{53}, a_{54} and a_{55} are the elements of matrix $\boldsymbol{A_5}$. And matrix $\boldsymbol{C}$ can be calculated by

$$\boldsymbol{C} = [\boldsymbol{C_1} \quad \boldsymbol{C_2} \quad \boldsymbol{C_3}] = \begin{bmatrix} c_{11} & c_{21} & c_{31} \\ c_{12} & c_{22} & c_{32} \\ c_{13} & c_{23} & c_{33} \\ c_{14} & c_{24} & c_{34} \\ c_{15} & c_{25} & c_{35} \end{bmatrix} \tag{15}$$

where $\boldsymbol{C_1}$, $\boldsymbol{C_2}$ and $\boldsymbol{C_3}$ are the submatrices of matrix $\boldsymbol{C}$. These three matrices all have a dimension of 5×1. In addition, it can be demonstrated that the elements in the matrices $\boldsymbol{A_5}$ and $\boldsymbol{C}$ satisfy the relationships such as $a_{53} = a_{54}$, $c_{21} = c_{31}$, $c_{22} = c_{32}$, $c_{23} = c_{34}$, $c_{24} = c_{33}$, and $c_{25} = c_{35}$. As a result, (16) can be obtained, which indicates that $f_{eB}(s)$ is equal to $f_{eC}(s)$. Therefore, the fault current introduced by the back-EMFs can be finally derived as (17).

$$f_{eB}(s) = \boldsymbol{A_5 C_2} \text{ and } f_{eC}(s) = \boldsymbol{A_5 C_3} \tag{16}$$

$$i_f(s) = [f_{eA}(s) - f_{eB}(s)]e_a(s) \tag{17}$$

Based on (17), it can be concluded that the fundamental component of the fault current is only determined by the back-EMF of the faulted phase, i.e., $e_a(s)$, and will not be affected by the back-EMFs of the other healthy phases, i.e., $e_b(s)$ and $e_c(s)$. $f_{eA}(s)$ and $f_{eB}(s)$ are derived from the matrixes $\boldsymbol{A_5}$ and $\boldsymbol{C}$ and the elements of these two matrixes are determined by the

matrixes $\boldsymbol{L}$ and $\boldsymbol{R}$ [see (2) and (3)] and the defined full rank matrixes $\boldsymbol{M_1}$ and $\boldsymbol{M_2}$ [see (A1)]. Therefore, the gains and poles of $f_{eA}(s)$ and $f_{eB}(s)$ are determined by the parameters of the machine (e.g., phase inductance, phase resistance, etc.) and the faulted turn ratio x. Since $f_{eA}(s)$ and $f_{eB}(s)$ are affected by the matrix $\boldsymbol{L}$, which accounts for the mutual inductances between the faulted turns and the healthy phases, such as M_{s35}, M_{s53}, M_{s45} and M_{s54} shown in (2), the fault current will also be influenced by these mutual inductances. This is different from the previous work in [25], which neglected these mutual inductances.

If $f_{eA}(s)$ and $f_{eB}(s)$ are determined, $[f_{eA}(s) - f_{eB}(s)]$ will be determined accordingly. In addition, the phase back-EMF under a given rotor speed can be easily calculated. As a result, for the PM machines with a certain faulted turn ratio x, the amplitude of the fundamental component of the fault current determined by the back-EMFs can be predicted using the equation (17).

B. PWM-Voltages Contributing to the Fault Current

Based on (9), the fault current introduced by the PWM voltages in s-domain can be derived as

$$i_f(s) = \begin{bmatrix}0\\0\\0\\0\\1\end{bmatrix}^T (s\boldsymbol{I} - \boldsymbol{A})^{-1}\boldsymbol{B}\begin{bmatrix}v_{Adsl}(s)\\v_{Bdsl}(s)\\v_{Cdsl}(s)\end{bmatrix} = \begin{bmatrix}f_A(s)\\f_B(s)\\f_C(s)\end{bmatrix}^T\begin{bmatrix}v_{Adsl}(s)\\v_{Bdsl}(s)\\v_{Cdsl}(s)\end{bmatrix} \quad (18)$$

where s is the Laplacian operator, and $\boldsymbol{I}$ is identity 5×5 matrix. $f_A(s)$, $f_B(s)$ and $f_C(s)$ are the transfer functions of the PWM voltages of the phases A, B and C, respectively. $v_{Adsl}(s)$, $v_{Bdsl}(s)$ and $v_{Cdsl}(s)$ are the PWM voltages in s-domain of the phases A, B and C, respectively.

If the 3-phase PWM voltages are the same such as $v_{dslA} = v_{dslB} = v_{dslC}$, the product of matrix $\boldsymbol{B}$ and $[1 \quad 1 \quad 1]^T$ is equal to a zero matrix with a dimension of 5×1, as

$$\boldsymbol{B}[1 \quad 1 \quad 1]^T V_s = [0 \quad 0 \quad 0 \quad 0 \quad 0]^T V_s \quad (19)$$

where V_s is the PWM voltage vector. In this case, the PWM ripple current introduced by the PWM voltages is equal to zero. Therefore, the sum of the transfer functions $f_A(s)$, $f_B(s)$ and $f_C(s)$ is equal to zero, as

$$i_f(s) = [f_A(s) + f_B(s) + f_C(s)]V_s = 0 \quad (20)$$

As it is assumed that the ITSC fault occurred in the phase A, the mutual inductances between the faulted turns and the phases B and C are the same. Therefore, $f_B(s)$ is equal to $f_C(s)$ and the relationship between $f_A(s)$, $f_B(s)$ and $f_C(s)$ is

$$f_A(s) = -2f_B(s) = -2f_C(s) \quad (21)$$

As a result, the fault current introduced by the PWM voltages can be expressed as

$$i_f(s) = \begin{bmatrix}f_A(s) & -\frac{1}{2}f_A(s) & -\frac{1}{2}f_A(s)\end{bmatrix}\begin{bmatrix}v_{Adsl}(s)\\v_{Bdsl}(s)\\v_{Cdsl}(s)\end{bmatrix} \quad (22)$$

Similarly, the PWM ripple component of the phase A introduced by the PWM voltages can be obtained such as

$$i_A(s) = \begin{bmatrix}f_{PA}(s) & -\frac{1}{2}f_{PA}(s) & -\frac{1}{2}f_{PA}(s)\end{bmatrix}\begin{bmatrix}v_{Adsl}(s)\\v_{Bdsl}(s)\\v_{Cdsl}(s)\end{bmatrix} \quad (23)$$

where $f_{PA}(s)$ is the transfer function of phase A PWM voltage.

C. Results and Discussions

For this investigated machine with a single turn short-circuit fault, the Bode diagram for $f_A(s)$, $f_{PA}(s)$ and $[f_{eA}(s) - f_{eB}(s)]$ can be obtained, as shown in Fig. 7. It can be found that when the frequency is lower than 100Hz, the back-EMF mainly contributes to the fundamental component of the fault current. The influence of the PWM voltages is negligibly small as the magnitude of $f_A(s)$ is much lower than that of $f_{eA}(s) - f_{eB}(s)$. This characteristic can be used to predict the amplitude of the fundamental fault current at relatively low frequency. In order to illustrate this, the predicted fault currents at low speed from 500rpm to 1500rpm corresponding to a frequency from 33.33Hz to 100Hz, has been calculated by using (17) and compared against the measure results, as shown in Fig. 5.

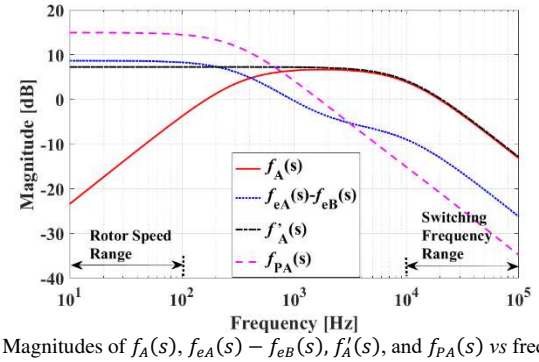

Fig. 7 Magnitudes of $f_A(s)$, $f_{eA}(s) - f_{eB}(s)$, $f'_A(s)$, and $f_{PA}(s)$ *vs* frequency of the investigated machine under a single turn short-circuited fault. $f'_A(s)$ will be described in detail in section IV.

TABLE II. SIMULATED RMS VALUE OF THE FUNDAMENTAL COMPONENT OF THE FAULT CURRENT *vs* Q-AXIS CURRENT.

Rotor speed	4500rpm (300Hz)			
d-axis current I_d (A)	0			
q-axis current I_q (A)	10	20	30	40
fault current I_F (A)	10.71	11.04	12.8	14.59

However, when the frequency is above 100Hz, both the PWM voltages and back-EMFs will contribute to the fundamental fault current. This is because the magnitudes of $f_A(s)$ cannot be neglected anymore, as shown in Fig. 7. To show this, it is assumed that the machine operates at high speed 4500rpm (corresponding to a frequency of 300Hz) with $I_d = 0$A but as I_q (from 10A to 40A). With different q-axis currents, it results in the changes in the fundamental component of the PWM voltages. However, as the prototype machine has a limited peak rotor speed of 1500rpm (100Hz), only simulated results provided, as shown in TABLE II. This is deemed acceptable as the accuracy of this proposed fault model has been fully validated in previous sections. It is found from TABLE II. that the RMS value of the fault current increases with increased I_q. In this case, if only back-EMF contributed to the fault current, the fault current would remain constant as back-EMF is unchanged for the same rotor speed. Therefore, one can conclude that the PWM voltages do contribute to the fault current. The higher the PWM voltages is, the larger the fault current will be.

IV. Investigation For the PWM Ripple Component of the Fault Current

A. Factors Affecting PWM Ripple Current

For the investigated machine with a single turn short-circuit fault, $f_A(s)$ can be obtained, which consists of five first-order systems. This is because the investigated machine is a fifth-order system, the transfer function $f_A(s)$ has five poles However, two of the five first-order systems have a gain of zero, so $f_A(s)$ can be simplified to (24). For the PWM ripple current, the first term of $f_A(s)$ can be regarded as the main contributor as its pole and gain is significantly larger than the other terms. This means that, to obtain the high frequency PWM ripple current, the second and third terms in the transfer function can be neglected. If so, $f_A(s)$ can be approximated to $f_A'(s)$, as shown in (25). This approximation method can be verified by Bode diagram, as shown in Fig. 7, where the magnitude of $f_A'(s)$ is almost the same as $f_A(s)$ at high frequency range (>2kHz).

$$f_A(s) = \frac{-94881}{(s+61909)} + \frac{3042}{(s+1737)} - \frac{356}{(s+1632)} \tag{24}$$

$$f_A'(s) = \frac{-94881}{(s+61909)} \tag{25}$$

$$i_f(s) = \begin{bmatrix} f_A'(s) & -\frac{1}{2}f_A'(s) & -\frac{1}{2}f_A'(s) \end{bmatrix} \begin{bmatrix} v_{Adsl}(s) \\ v_{Bdsl}(s) \\ v_{Cdsl}(s) \end{bmatrix} \tag{26}$$

$$\begin{bmatrix} i_{ai}(s) \\ i_{bi}(s) \\ i_{ci}(s) \end{bmatrix} = \frac{2}{3}\frac{1}{L_i s + R_i} \left\{ \begin{bmatrix} 1 & -\frac{1}{2} & -\frac{1}{2} \\ -\frac{1}{2} & 1 & -\frac{1}{2} \\ -\frac{1}{2} & -\frac{1}{2} & \frac{2}{2} \end{bmatrix} \begin{bmatrix} v_{Adsl}(s) \\ v_{Bdsl}(s) \\ v_{Cdsl}(s) \end{bmatrix} \right\} \tag{27}$$

where $i_{ai}(s)$, $i_{bi}(s)$, and $i_{ci}(s)$ are the 3-phase currents for a 3-phase impedance loads. L_i and R_i are the inductance and resistance of the 3-phase impedance load.

The PWM ripple component of the fault current introduced by the PWM voltages of this investigated machine can be derived as (26), which is a high frequency model, and is similar to that of the phase A current under healthy condition, as illustrated in (27). If L_i and R_i in (27) are equal to 7μH and 0.435Ω, respectively, $i_{ai}(s)$ will be the same as $i_f(s)$. Therefore, the factors influencing the PWM ripple component of the phase current will have a similar impact on the PWM ripple component of the fault current. As a result, the DC bus voltage and switching frequency, two factors often affecting the PWM current ripple in phase current, will also affect the PWM current ripple in the fault current. In addition, if the faulted turn ratio x or coil connections (series or parallel) is changed, $f_A'(s)$ will be changed accordingly. This in turn leads to the changes in the PWM ripple current.

Based on the analysis above, it can be concluded that the PWM ripple current is mainly affected by factors such as DC bus voltage, switching frequency, number of short-circuited turns and coils connection, which will be investigated in detail in the following sections.

B. DC Bus Voltage

The simulations and experiments with the same switching frequency (20kHz) and modulation strategy (SVPWM) but with different DC bus voltages have been carried out to investigate the influence of the DC bus voltage on the PWM ripple current, and the simulated and measured results are shown in Fig. 8. When the fundamental fault current reaches its peak value, the PWM ripple current within 4 PWM cycles is extracted to clearly show the difference in terms of PWM ripple current, as illustrated in Fig. 8. When the DC bus voltage changes from 24V to 36V, PWM ripple current increases accordingly both in the simulated and measured results. This indicates that the higher the DC bus voltage is, the larger the PWM ripple current will be. It is also found from Fig. 8 that there is a good agreement between the simulated and measured results, which further demonstrates the accuracy of the proposed fault model.

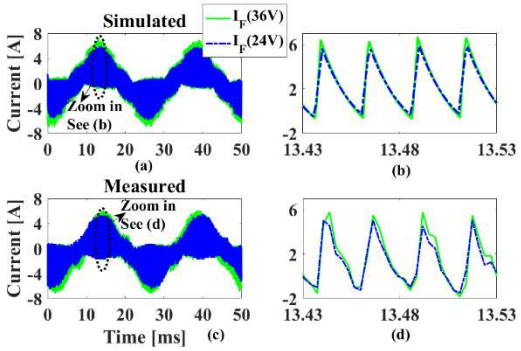

Fig. 8 Simulated and measured fault currents for different DC bus voltages. The rotor speed is 600rpm and the demand currents are i_d = 0A and i_q = 10A.

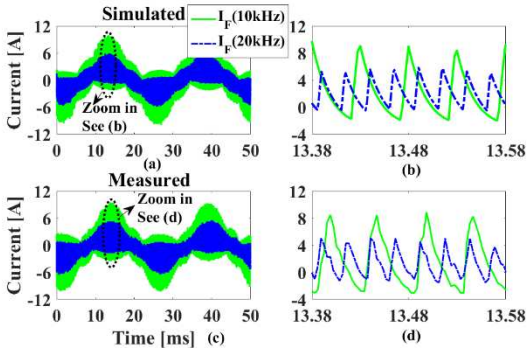

Fig. 9 Simulated and measured fault currents for different switching frequencies. The rotor speed is 600rpm and the demand currents are i_d = 0A and i_q = 10A.

C. Switching Frequency

In addition to the DC bus voltage, different PWM period (T_s) or switching frequency will also affect the PWM ripple current. To validate the conclusion regarding the impact of switching frequency on the PWM ripple current, simulations and experiments with 2 different frequencies such as 10kHz and 20kHz have been carried out in this section. For these simulations and experiments, the DC bus voltage (24V) and the modulation strategy (SVPWM) are kept the same. The simulated and measured fault currents are shown in Fig. 9. Again, the PWM ripple currents within 4 PWM cycles around the peak value of its corresponding fundamental fault currents have been extracted, as shown in Fig. 9. It is observed that the

PWM ripple current is sensitive to the change in switching frequency. And both the simulated and measured results show that the higher the switching frequency is, the lower the PWM ripple current content will be. Although not shown here, this conclusion can also be applicable to the phase current.

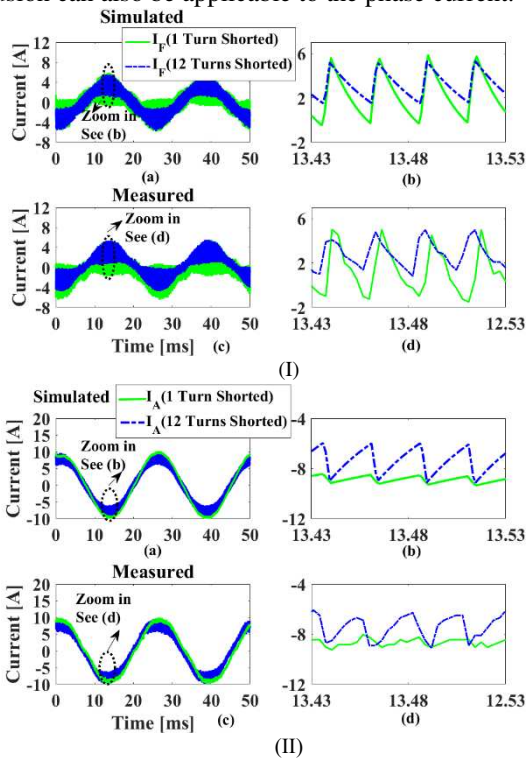

Fig. 10 Simulated and measured (I) fault currents and (II) phase A current for different numbers of short-circuited turns. The rotor speed is 600rpm and the demand currents are i_d = 0A and i_q = 10A.

D. Number of Short-Circuited Turns

In addition to the DC bus voltage and switching frequency, the number of short-circuited turns is another major factor contributing to the PWM ripple components of the fault and phase currents. To clearly show this, two simulations and experiments with one turn and twelve turns short-circuited have been carried out, and the results for both the fault and phase currents are shown in Fig. 10. Both the simulated and measured results in Fig. 10 (a) indicate that when the number of short-circuited turns increases, the PWM ripple component in the fault current reduces. However, it is opposite for the phase current, as shown in Fig. 10 (b). This is because the poles and gains of $f_A(s)$ [see (22)] and $f_{PA}(s)$ [see (23)] change with different faulted turn ratios x. To demonstrate this, one turn and twelve turns short-circuited faults are taken as example and the changes in the magnitudes of $f_A(s)$ and $f_{PA}(s)$ by using Bode diagrams are shown in Fig. 11. For the fault current, when the number of short-circuited turns increases, the inductances and resistances in the fault circuit loop will be increased, resulting in decreased gains of $f_A(s)$ at twice the switching frequency (i.e., 20kHz), as illustrated in Fig. 11. However, for the phase current, with the number of short-circuited turns increases, the inductance and resistance in the remaining healthy part of the phase A winding reduce, resulting in significantly increased gains of $f_{PA}(s)$ at twice the switching frequency (i.e., 20kHz), as illustrated in Fig. 11. The lower the gains of $f_A(s)$ and $f_{PA}(s)$ at 20kHz, the smaller the PWM ripple components in the fault and phase currents.

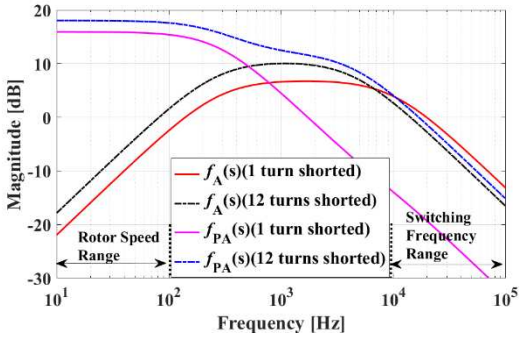

Fig. 11 Magnitudes of $f_A(s)$ and $f_{PA}(s)$ *vs* frequency for different numbers of short-circuited turns.

E. Coils Connected in Series and Parallel

Similar to the number of short-circuited turns, different coil connections, i.e., series connection or parallel connection, will result in different machine parameters, particularly the inductance and resistance. As a result, different coil connections will have a significant impact on the PWM ripple component in the fault current. To clearly illustrate this, a comparison of fault currents for coils connected in series and parallel has been carried out, the simulated and measured results are shown in Fig. 12. Here the same set of demand current (i_d = 0A and i_q = 10A) and the same DC bus voltage (24V) have been used for both coil connections. In addition, the rotor speed is 600rpm and the switching frequency is 20kHz. The PWM ripple currents within 4 PWM cycles around the corresponding peak fundamental fault currents have been extracted, as shown in Fig. 12. It is found from both the simulated and measured results that when the coils are connected in parallel, the PWM ripple current is much larger than that when the same coils are connected in series.

Using similar method as for the coils connected in parallel, $f_A'(s)$ for the coils connected in series with a single turn short-circuited fault in a_1 can be calculated by (28). It is found that the pole and gain in (28) are much smaller than those in (25). This means that the PWM ripple current in series coils will be lower than that of parallel coils, which can be further validated by the Bode diagram, as shown in Fig. 13.

$$f_A'(s) = \frac{-27851}{(s + 39682)} \tag{28}$$

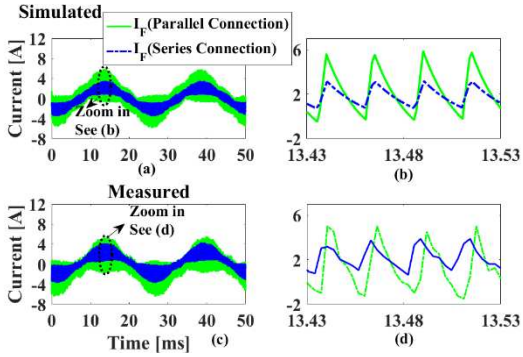

Fig. 12 Simulated and measured fault currents for coils connected in series and in parallel. The rotor speed is 600rpm and the demand currents are i_d = 0A and i_q = 10A.

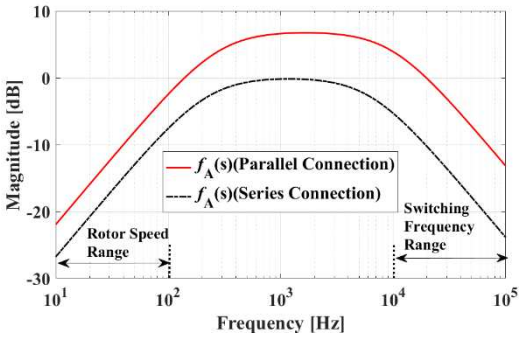

Fig. 13 Magnitude of $f_A(s)$ *vs* frequency with different coil connections.

V. Conclusion

This paper presents a novel PWM voltage-based fault model for PM machines with ITSC faults that can account for the PWM harmonics in the fault current. As a result, compared with the existing models in literature using sinewave voltages as inputs to the PM machines, the simulated fault currents from this developed model are much closer to the measured ones. In addition, the investigations in this paper have shown that the PWM harmonics could be more than 50% of the fundamental component. If these PWM harmonics are neglected, it would result in serious underestimation of the thermal stress under ITSC fault.

Based on the developed fault model, the influence of back-EMF and PWM voltages on the fundamental component of fault current has been investigated separately. It is found that, at lower speed, only the back-EMF contributes to the fundamental component of fault current. However, as speed increases, both back-EMF and PWM voltages will affect the fundamental component of fault current. In addition, factors affecting the PWM ripple current have been explored. Findings of this paper have shown that the PWM ripple current increases with increased DC bus voltage, but it reduces when switching frequency or number of short-circuited turns increases. In addition, with the same faulted turn ratio, coils connected in parallel will have much larger PWM ripple component in the fault current than coils connected in series.

Appendix

Two matrixes with full rank are defined as $\boldsymbol{M_1}$ and $\boldsymbol{M_2}$ in (A1). Meanwhile, the relevant linear transformation is depicted in (A2). With (A1) and (A2), (5) can be further derived as (A3). As a result, the product of matrices in front of the current and voltage vectors can be simplified, as illustrated by (A5), (A6), (A7) and (A8).

$$\boldsymbol{M_1}=\begin{bmatrix} \frac{2}{3} & \frac{2}{3} & -\frac{1}{3} & -\frac{1}{3} & 0 \\ 0 & 0 & \frac{\sqrt{3}}{3} & -\frac{\sqrt{3}}{3} & 0 \\ 1 & 0 & 0 & 0 & 0 \\ 0 & 0 & 0 & 0 & 1 \\ \frac{1}{4} & \frac{1}{4} & \frac{1}{4} & \frac{1}{4} & 0 \end{bmatrix} \text{ and } \boldsymbol{M_2}=\begin{bmatrix} \frac{2}{3} & -\frac{1}{3} & -\frac{1}{3} \\ 0 & \frac{\sqrt{3}}{3} & -\frac{\sqrt{3}}{3} \\ \frac{1}{3} & \frac{1}{3} & \frac{1}{3} \end{bmatrix} \tag{A1}$$

$$\begin{bmatrix} i_\alpha \\ i_\beta \\ i_\gamma \\ i_\delta \\ i_0 \end{bmatrix}=\boldsymbol{M_1}\begin{bmatrix} i_{p1} \\ i_{p2} \\ i_b \\ i_c \\ i_f \end{bmatrix}\begin{bmatrix} e_\alpha \\ e_\beta \\ e_0 \end{bmatrix}=\boldsymbol{M_2}\begin{bmatrix} e_a \\ e_b \\ e_c \end{bmatrix} \text{ and } \begin{bmatrix} v_\alpha \\ v_\beta \\ v_0 \end{bmatrix}=\boldsymbol{M_2}\begin{bmatrix} v_{dslA} \\ v_{dslB} \\ v_{dslC} \end{bmatrix} \tag{A2}$$

where i_α, i_β, i_γ, i_δ and i_0 denote the new current vectors converted from i_{p1}, i_{p2}, i_b, i_c and i_f and matrix $\boldsymbol{M_1}$. e_α, e_β, and e_0 represent the back-EMF vectors obtained from e_a, e_b, and e_c and $\boldsymbol{M_2}$ by linear transformation. v_α, v_β, and v_0 are the voltages from the transformation of the PWM voltages, and the already defined matrix $\boldsymbol{M_2}$.

$$\boldsymbol{P_1 L M_1}^{-1}\frac{d}{dt}\begin{bmatrix} i_\alpha \\ i_\beta \\ i_\gamma \\ i_\delta \\ i_0 \end{bmatrix}=-\boldsymbol{P_1 R M_1}^{-1}\begin{bmatrix} i_\alpha \\ i_\beta \\ i_\gamma \\ i_\delta \\ i_0 \end{bmatrix}+\boldsymbol{P_1}\begin{bmatrix} 1 & 0 & 0 \\ 1 & 0 & 0 \\ 0 & 1 & 0 \\ 0 & 0 & 1 \\ 0 & 0 & 0 \end{bmatrix}\boldsymbol{M_2}^{-1}\begin{bmatrix} v_\alpha \\ v_\beta \\ v_0 \end{bmatrix}-\boldsymbol{P_1}\begin{bmatrix} 1-x & 0 & 0 \\ 1 & 0 & 0 \\ 0 & 1 & 0 \\ 0 & 0 & 1 \\ x & 0 & 0 \end{bmatrix}\boldsymbol{M_2}^{-1}\begin{bmatrix} e_\alpha \\ e_\beta \\ e_0 \end{bmatrix} \tag{A3}$$

$$\boldsymbol{M_1 P_1 L M_1}^{-1}=\begin{bmatrix} \boldsymbol{L_{4\times4}} & \boldsymbol{L_{4\times1}} \\ \boldsymbol{0_{1\times4}} & 0 \end{bmatrix} \tag{A4}$$

$$\boldsymbol{M_1 P_1 R M_1}^{-1}=\begin{bmatrix} \boldsymbol{R_{4\times4}} & \boldsymbol{R_{4\times1}} \\ \boldsymbol{0_{1\times4}} & 0 \end{bmatrix} \tag{A5}$$

$$\boldsymbol{M_1 P_1}\begin{bmatrix} 1 & 0 & 0 \\ 1 & 0 & 0 \\ 0 & 1 & 0 \\ 0 & 0 & 1 \\ 0 & 0 & 0 \end{bmatrix}\boldsymbol{M_2}^{-1}=\begin{bmatrix} \boldsymbol{V_{4\times2}} & \boldsymbol{0_{4\times1}} \\ \boldsymbol{0_{1\times2}} & 0 \end{bmatrix} \tag{A6}$$

$$\boldsymbol{M_1 P_1}\begin{bmatrix} 1-x & 0 & 0 \\ 1 & 0 & 0 \\ 0 & 1 & 0 \\ 0 & 0 & 1 \\ x & 0 & 0 \end{bmatrix}\boldsymbol{M_2}^{-1}=\begin{bmatrix} \boldsymbol{E_{4\times2}} & \boldsymbol{E_{4\times1}} \\ \boldsymbol{0_{1\times2}} & 0 \end{bmatrix} \tag{A7}$$

where $\boldsymbol{L_{4\times4}}$ is an inductance matrix with a dimension of 4×4. It is converted by linear transformation from the matrix $\boldsymbol{L}$, the previously defined matrix $\boldsymbol{M_1}$ and its inverse matrix $\boldsymbol{M_1}^{-1}$, and the matrix $\boldsymbol{P_1}$. $\boldsymbol{L_{4\times1}}$ is an inductance matrix with a dimension of 4×1, which is extracted from the fifth column of the products of matrices $\boldsymbol{M_1}$, $\boldsymbol{P_1}$, $\boldsymbol{L}$ and $\boldsymbol{M_1}^{-1}$. $\boldsymbol{R_{4\times4}}$ is a resistance matrix with a dimension of 4×4, which is the first four rows and columns of the products of matrices $\boldsymbol{M_1}$, $\boldsymbol{P_1}$, $\boldsymbol{R}$ and $\boldsymbol{M_1}^{-1}$. $\boldsymbol{R_{4\times1}}$ is a resistance matrix with a dimension of 4×1. $\boldsymbol{V_{4\times2}}$ is a numerical matrix with a dimension of 4×2. $\boldsymbol{E_{4\times4}}$ is an identity matrix with a dimension of 4×4. $\boldsymbol{0_{1\times4}}$ and $\boldsymbol{0_{1\times2}}$ are matrices with a dimension of 1×4 and 1×2, respectively, and the elements in these two matrices are all equal to zero.

References

[1] V. Nguyen, D. W. Wang, J. Seshadrinath, A. Ukil, M. S. Krishna, S. Nadarajan, and V. Vaiyapuri, "A method for incipient interturn fault detection and severity estimation of induction motors under inherent asymmetry and voltage imbalance," *IEEE Trans. Transp. Electrific.,* vol. 3, no. 3, pp. 703-715, 2017.

[2] L. Liu, K. Wang, L. L. Guo and J. Li, "Analysis of Inter-turn Short Circuit Faults in Dual Three-Phase PMSM for Electromechanical Actuator," *IEEE Trans. Transp. Electrific.*, 2023, Early Access.

[3] V. Gurusamy, G. A. Capolino, B. Akin, H. Henao, R. Romary and R. Pusca, "Recent Trends in Magnetic Sensors and Flux-Based Condition Monitoring of Electromagnetic Devices," *IEEE Trans Ind Appl,* vol. 58, no. 4, pp. 4668-4684, Aug. 2022.

[4] J. Y. Zhang, W. Zhan and M. Ehsani, "Diagnosis and Fault-Tolerant Control of Permanent Magnet Synchronous Motors With Interturn Short-Circuit Fault," *IEEE Trans. Control Syst. Technol.,* 2023, Early Access.

[5] P. Arumugam, C. Gerada, T. Hamiti, C. Hill, and S. Bozhko, "A review on turn-turn short circuit fault management," in *Proc. Int. Conf. Electr. Syst. Aircr., Railway, Ship Propulsion Road Veh*., 2015, pp. 1–5.

[6] J. Hang, W. Sun, Q. Hu, X. Ren, and S. Ding, "Integration of Interturn Fault Diagnosis and Fault-Tolerant Control for PMSM Drive System," *IEEE Trans. Transp. Electrific.,* vol. 8, no. 2, pp. 2825-2835, 2021.

[7] J. Faiz and H. Nejadi-Koti, "Demagnetization fault indexes in permanent magnet synchronous motors—An overview," *IEEE Trans. Magn.*, vol. 52, no. 4, pp. 1-11, 2015.

[8] S. Moon, H. Jeong, H. Lee, and S. W. Kim, "Detection and classification of demagnetization and interturn short faults of IPMSMs," *IEEE Trans. Ind. Electron.,* vol. 64, no. 12, pp. 9433-9441, 2017.

[9] H. Chen, C. H. Fang, J. L. Dong, S. L. Lu, V. Pires, J. Martins, and M. P. Aguirre, "Diagnosis of Inter-turn Short-Circuit of SRM Based on Ratio of Current Components", *IEEE Trans. Transp. Electrific.*, 2022, Early Access.

[10] Z. Xu, J. Zhang, J. Xiong, Y. Wu, and M. Cheng, "An Improved High Frequency Voltage Injection Method for Inter-turn Short-circuit Fault Detection in PMSMs," *IEEE Trans. Transp. Electrific.*, 2022, Early Access.

[11] H. Zhou, W. Zhao, G. Liu, R. Cheng, and Y. Xie, "Remedial field-oriented control of five-phase fault-tolerant permanent-magnet motor by using reduced-order transformation matrices," *IEEE Trans. Ind. Electron.*, vol. 64, no. 1, pp. 169-178, Jan. 2017.

[12] F. Wu, P. Zheng, and T. M. Jahns, "Analytical modeling of interturn short circuit for multiphase fault-tolerant PM machines with fractional slot concentrated windings," *IEEE Trans. Ind. Appl.,* vol. 53, no. 3, pp. 1994-2006, 2017.

[13] L. S. Maraaba, Z. M. Al-Hamouz, and M. A. Abido, "Mathematical modeling, simulation and experimental testing of interior-mount LSPMSM under stator inter-turn fault," *IEEE Trans. Energy Convers.*, vol. 34, no. 3, pp. 1213-1222, 2018.

[14] I. Jeong, B. J. Hyon, and K. Nam, "Dynamic modeling and control for SPMSMs with internal turn short fault," *IEEE Trans. Power Electron*., vol. 28, no. 7, pp. 3495-3508, Jul 2013.

[15] B. Gu, J. H. Choi, and I. Jung, "Development and analysis of interturn short fault model of PMSMs with series and parallel winding connections," *IEEE Trans. Power. Electron.*, vol. 29, no. 4, pp. 2016-2026, April 2014.

[16] J. A. Farooq, T. Raminosoa, A. Djerdir, and A. J. Miraoui, "Modelling and simulation of stator winding inter-turn faults in permanent magnet synchronous motors," *COMPEL-Int. J. Comput. Elect. Electron. Eng.,* vol. 27, no. 4, pp. 887-896, 2008.

[17] L. Romeral, J. C. Urresty, J. R. Ruiz, and A. G. Espinosa, "Modeling of surface-mounted permanent magnet synchronous motors with stator winding interturn faults," *IEEE Trans. Ind. Electron*., vol. 58, no. 5, pp. 1576-1585, 2010.

[18] C. Rojas, M. Melero, M. Cabanas, J. Cano, G. Orcajo, and F. Pedrayes, "Finite element model for the study of inter-turn short circuits in induction motors," *IEEE International Symposium on Diagnostics for Electric Machines, Power Electronics and Drives*, 2007, pp. 415-419.

[19] M. Fitouri, Y. Bensalem, and M. N. Abdelkrim, "Modeling and detection of the short-circuit fault in PMSM using Finite Element Analysis," *IFAC-PapersOnLine*, vol. 49, no. 12, pp. 1418-1423, 2016.

[20] Y. S. Lee, K. T. Kim, and J. J. Hur, "Finite-element analysis of the demagnetization of IPM-type BLDC motor with stator turn fault," *IEEE Trans. Magn.*, vol. 50, no. 2, pp. 889-892, 2014.

[21] B. Sen, J. B. Wang, and P. Lazari, "A detailed transient model of interior permanent magnet motor accounting for saturation under stator turn fault," in *IEEE ECCE*, 2013, pp. 3548-3555.

[22] A. Fatemi, D. M. Ionel, N. A. Demerdash, and T. W. Nehl, "Optimal design of IPM motors with different cooling systems and winding configurations," *IEEE Trans Ind Appl*., vol. 52, no. 4, pp. 3041-3049, 2016.

[23] G. Du, W. Ye, Y. Zhang, L. Wang, T. Pu, and N. J. Huang, "Comprehensive Analysis of the AC Copper Loss for High Speed PM Machine With Form-Wound Windings," *IEEE Access*, vol. 10, pp. 9036-9047, 2022.

[24] S. Inamura, T. Sakai, and K. J. M. Sawa, "A temperature rise analysis of switched reluctance motor due to the core and copper loss by FEM," *IEEE Trans. Magn.*, vol. 39, no. 3, pp. 1554-1557, 2003.

[25] Y. Xu, Z. Zhang, Y. Jiang, J. Huang, and W. Jiang, "Numerical Analysis of Turn-to-Turn Short Circuit Current Mitigation for Concentrated Winding Permanent Magnet Machines With Series and Parallel Connected Windings," *IEEE Trans. Ind. Electron.,* vol. 67, no. 11, pp. 9101-9111, 2019.